Characterization of hot electrons generated by laser–plasma interaction at shock ignition intensities

View Online   Export Citation   CrossMark

E. D. Filippov,[1,a)] [iD] M. Khan,[2] [iD] A. Tentori,[3] [iD] P. Gajdos,[4] [iD] A. S. Martynenko,[1,5] [iD] R. Dudzak[4,6] [iD]
P. Koester,[7] [iD] G. Zeraouli,[8] [iD] D. Mancelli,[9,10] [iD] F. Baffigi,[7] [iD] L. A. Gizzi[7] [iD] S. A. Pikuz,[1,11] [iD] Ph.D. Nicolaï,[3]
N. C. Woolsey,[2] [iD] R. Fedosejevs,[12] [iD] M. Krus,[4] [iD] L. Juha,[6] [iD] D. Batani,[3] [iD] O. Renner,[4,6,13] [iD]
and G. Cristoforetti[7] [iD]

AFFILIATIONS

[1]Joint Institute for High Temperatures RAS, Moscow 125412, Russia
[2]York Plasma Institute, School of Physics, Engineering and Technology, University of York, York YO10 5DD, United Kingdom
[3]Université de Bordeaux, CNRS, CEA, CELIA, Talence 33405, France
[4]Institute of Plasma Physics of the CAS, Prague, Czech Republic
[5]Plasma Physics Department, GSI Helmholtzzentrum für Schwerionenforschung, 64291 Darmstadt, Germany
[6]Institute of Physics of the CAS, Prague, Czech Republic
[7]Intense Laser Irradiation Laboratory, INO-CNR, Pisa 56124, Italy
[8]Centro de Laseres Pulsados (CLPU), Edicio M5, Parque Científico. C Adaja, 8, Salamanca 37185, Spain
[9]Institute of Plasma Physics and Lasers - IPPL, Centre of Research and Innovation, Hellenic Mediterranean University, Rethymnon, Greece
[10]Department of Electronic Engineering, Hellenic Mediterranean University, Chania, Greece
[11]National Research Nuclear University MEPhI, Moscow 115409, Russia
[12]University of Alberta, Edmonton T6G 2V4, Alberta, Canada
[13]The Extreme Light Infrastructure ERIC, ELI Beamlines Facility, Dolní Břežany, Czech Republic

[a)]Author to whom correspondence should be addressed: edfilippov@ihed.ras.ru

ABSTRACT

In an experiment carried out at the Prague Asterix Laser System at laser intensities relevant to shock ignition conditions ($I > 10^{16}$ W/cm^2), the heating and transport of hot electrons were studied by using several complementary diagnostics, i.e., K$_\alpha$ time-resolved imaging, hard x-ray filtering (a bremsstrahlung cannon), and electron spectroscopy. Ablators with differing composition from low Z (parylene N) to high Z (nickel) were used in multilayer planar targets to produce plasmas with different coronal temperature and collisionality and modify the conditions of hot-electron generation. The variety of available diagnostics allowed full characterization of the population of hot electrons, retrieving their conversion efficiency, time generation and duration, temperature, and angular divergence. The obtained results are shown to be consistent with those from detailed simulations and similar inertial confinement fusion experiments. Based on the measured data, the advantages, reliability, and complementarity of the experimental diagnostics are discussed.

I. INTRODUCTION

Shock ignition (SI) is a state-of-the-art high-gain scheme to direct-drive inertial confinement fusion (ICF), in which a strong converging shock is launched at the end of the compression phase to ignite the fuel.[1–4] The strong shock is triggered by a short intense laser spike (300–500 ps) with an intensity of ~10^{16} W/cm². Therefore, the success of the SI concept depends on efficient coupling of the laser spike with the extended plasma corona surrounding the imploding envelope. However, in this interaction regime, the nonlinear growth of parametric instabilities[5–7] and the resulting generation of hot electrons (HEs)[8–11] can play an important role in the laser–plasma coupling. The latter can be detrimental if the electrons are too energetic and preheat the fuel, as in the conventional ICF approach, but if they are insufficiently energetic, they cannot penetrate the compressed fuel and can even increase the shock pressure, which would facilitate fuel ignition.[12] Therefore, a detailed understanding of HE generation under SI plasma conditions is required, but this is hampered by the difficulty of performing a full-scale SI experiment with the laser facilities currently available. Moreover, because of the high nonlinearity of the processes, extrapolation of experimental results obtained at lower laser intensities[13–15] and typically colder plasmas may lead to incorrect conclusions.[16] Meanwhile, numerical 2D particle-in-cell simulations are valuable for identifying the interplay of physical mechanisms and plasma parameters that influence these processes, but they are usually limited to a few picoseconds of interaction, which is much shorter than the ignition spike.[17] To quantify the impact of HEs on the fuel compression and plasma hydrodynamics, specific modules have been implemented into hydrodynamic codes to evaluate the growth of parametric instabilities, the generation of HEs, and the energy deposition into the plasma.[18] This approach determines the parameters with correct orders of magnitude, but their validity is limited because the calculations simply implement scaling laws obtained from experiments carried out at lower laser intensities.

In addition to the difficulty of performing experiments under full-scale SI conditions, the characterization of HEs propagating into the plasma is often made difficult by the limitations of experimental geometry and diagnostics. To simplify the diagnostic setup and provide better lines of sight, most of these laser–plasma experiments are usually carried out in a planar geometry by using flat targets. This geometry allows the use of various diagnostic tools for characterizing the HEs and the laser–plasma interaction (LPI), including ultrafast x-ray imaging,[19,20] x-ray and optical spectroscopy,[15,21–23] angular filter refractometry,[24] and particle time-of-flight methods[20,25] (e.g., electron spectrometers with strong magnetic field or neutron diagnostics).

When foil targets with a thickness of a few tens of micrometers are considered, electron magnetic spectrometers (designated herein with the label ES) located behind the target can be used, allowing direct measurements of the electron energy distribution function (EEDF) for the laser-generated source, which is crucial in ICF experiments.[26–28] However, these spectrometers only detect the most-energetic electrons that can propagate through the target and escape from its rear side. In fact, some HEs undergo multiple collisions into the target, dissipating either some or all of their energy; consequently, their signature in the ES spectra acquired behind the target is either missing or down-shifted in energy.

Incidentally, a significant fraction of the electrons that are expected to preheat the ICF fuel in a full-scale SI reactor are usually trapped because of induced charge separation and "recirculate" into the target, thereby preventing their detection by these detectors. On the other hand, the dissipation of energy of low-energy electrons into the target produces secondary x rays that can be measured by various techniques. Typical diagnostic tools include x-ray spectroscopy and imaging,[29] which offer spatial and temporal information about HE transport into the target and allow retrieval of the energy spectrum of the electron source. However, characterizing HEs by using x-ray tools implies assumptions about the spatial geometry of the source or the EEDF characteristics; moreover, it requires modeling the HE propagation through an ionized target, which is not yet fully understood. These factors result in the obtained results having considerable uncertainty.

Overall, from the situation described above, it is evident that each diagnostic can measure only a fraction of the HEs, depending on their energy, the target composition, and the propagation geometry; this should be accounted for when comparing different experiments, and it can explain some of the discrepancies observed. This also suggests that a combined approach is desirable to achieve a reliable characterization of the full HE source, which is needed to estimate the effects on the heating of the cold fuel. Herein, we report the results of an experiment at the Prague Asterix Laser System (PALS)[30] facility, aimed at characterizing HEs generated at laser intensities relevant to SI. We compare the results of different HE diagnostics, including time-resolved K_α imaging and hard x-ray bremsstrahlung and electron spectroscopy, showing correlations among them and discussing critically their advantages and disadvantages.

II. EXPERIMENTAL SETUP AND METHODS

The experiment reported herein was conducted at PALS,[30] a joint facility of the Institutes of Physics and Plasma Physics of the Czech Academy of Sciences. A multilayer target was irradiated (Fig. 1) at normal incidence by a laser pulse with an energy of ~600 J and a duration of ~300 ps to study the generation of HEs at a laser intensity typical of SI. Operating at the fundamental wavelength of 1.315 μm, the laser beam was smoothed by a random phase plate and focused to a Gaussian spot with a FWHM of ~100 μm, resulting in a peak intensity on the target of ~1.5×10^{16} W/cm². The target structure used in the experiment is shown in Fig. 1, the main difference among the targets being the material of the ablation layer forming the plasma corona, which was a 20 μm-thick flat layer of pure aluminum, carbon (polycrystalline graphite with a density of ~1 g/cm³), titanium, nickel, or parylene N (CH), the latter coated with a thin Al layer (40 nm). Behind the ablation layer was a 50 μm layer of polypropylene (PP) in which the HEs generated by LPI could propagate, followed by a 10 μm layer of copper used as a tracer of HEs by the time-resolved K_α imaging technique (see below). Finally, a 20 μm layer of parylene N was used to reduce the effect of HE recirculation into the Cu layer.

Using targets with different compositions was done to investigate the effects of the ablator on the extent of parametric instabilities and the HE conversion efficiency and temperature.[15,31] See Ref. 32 for a detailed characterization and discussion of LPI. Herein,
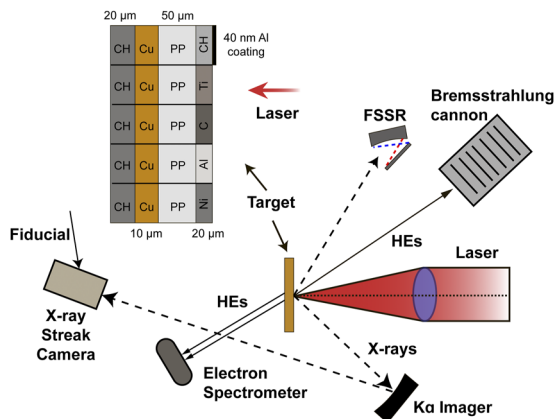
FIG. 1. Schematic of experimental setup and target design. In the experiment, a solid layered target with a choice for the ablation layer is irradiated by an intense laser pulse, and diagnostics involving an x-ray time-resolved Cu K$_\alpha$ imager and time-integrated Cu K$_\alpha$ spectrometer, ESs, and a BSC are used simultaneously. The Cu K$_\alpha$ imager comprises a spherically bent quartz crystal combined with an x-ray streak camera synchronized with a frequency-tripled pickoff of the heating laser.

we show and discuss results pertaining to the laser-driven source of HEs. In addition to using time-resolved K$_\alpha$ imaging and spectroscopy, the HEs were characterized using a time-integrated x-ray continuum spectrometer [bremsstrahlung cannon (BSC)] based on differential filtering[28,33–35] and three ESs deployed in front of and behind the target.[27]

A. K$_\alpha$ time- and 1D-space-resolved imaging

Time-resolved K$_\alpha$ imaging was used to measure the K$_{\alpha1}$ emission from copper (λ = 1.5406 Å) heated by HEs generated in the ablation layer. For this purpose, a spherically bent round quartz crystal (422) (R = 500 mm) arranged at an almost normal angle of incidence was used. The entrance window of the crystal had a

diameter of d = 24 mm, resulting in a corresponding spectral window of 1.4 mÅ limited by the edges of the crystal. X rays were detected by a Hamamatsu C13410-06 x-ray streak camera (designated herein with the label XRS), whose cathode was placed close to the meridian focus for the imaging scheme, with instrumental spectral broadening playing a negligible role. The XRS slit in front of the cathode was positioned horizontally, so that the lateral coordinate of the signal into the XRS image (i.e., the x axis) indicated the spatial extent of the HEs emitting area which was practically not affected by the crystal rocking curve; the spatial resolution was limited to ~4 μm by the XRS pixel size, as recalculated to the source position. The vertical coordinate (i.e., the y axis) was related to the temporal evolution. A typical XRS image measured in the experiment is shown in Fig. 2(a), while the spectral window of the measured spectrum is shown in Fig. 2(b) together with simulated K$_\alpha$ x-ray spectra emitted by Cu targets at different temperatures. Assuming that the bulk temperature of the Cu layer is no more than a few tens of electron-volts,[34] the spectral window overlaps well with the Cu K$_{\alpha1}$ line [see Fig. 2(b)]; however, for higher bulk temperature, the line contour broadens significantly to exceed the natural width of ~0.46 mÅ,[36] and so the instrumental spectral width samples only a portion of the K$_\alpha$ emission. The entrance slit of the XRS was filtered by a 10 μm aluminum foil to prevent the optical radiation of the laser plasma from reaching the camera. A thick lead screen was also located in the line of sight from the target to the slit to protect the XRS from direct x rays and hot particles generated during the laser interaction.

Cu K$_{\alpha1}$ emission was detected with a temporal smearing of ~33 ps due to the slit width. The absolute timing of the K$_\alpha$ emission was made possible by using a frequency-tripled pick-off of the main laser beam as a time fiducial. See Ref. 37 for a detailed description of the absolute time calibration. Using this method, the absolute delay between the impact of the laser on the target and the generation of the K$_\alpha$ emission was measured with an uncertainty of 45 ps, taking into account the overall experimental jitter and temporal profile fitting. The intensity calibration of the imager was performed by comparing the total integral flux on the XRS with the signal measured on an absolutely calibrated Fuji SR-type imaging plate (IP)[38] positioned in front of the XRS cathode. The transfer function of the
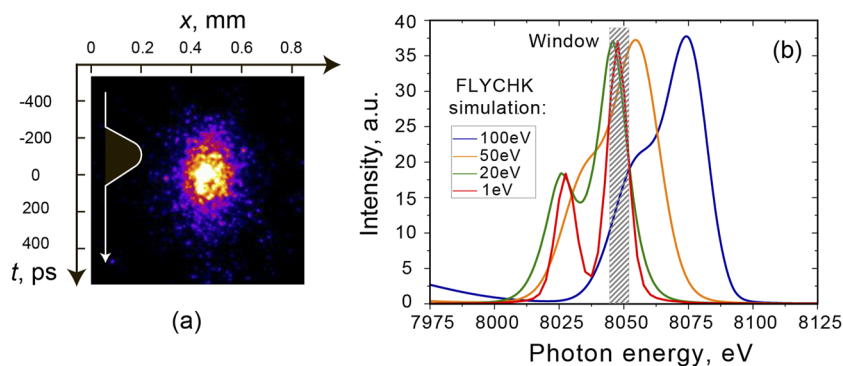

FIG. 2. (a) Example of x-ray streak camera (XRS) image measured in experiment. The white arrowed line in the image shows the laser profile, and the spatial scale is given for the detector plane at magnification M = 4 of the optical scheme. (b) Simulated K$_\alpha$ emission profiles obtained for different temperatures of Cu layer. The simulations were performed using the FLYCHK code with 30 keV electrons added at a level of 0.01% to stimulate the K$_\alpha$ excitation. The dashed gray region indicates the spectral window of the imager.

imager spectrometer and the filter transmission for a given setup were also considered.

B. Bremsstrahlung cannon

Indirect information about the amount and energy of the generated HEs was obtained using a BSC, which is a hard x-ray spectrometer that measures x rays emitted during laser–matter interaction in a broad spectral range.[34] The BSC was positioned at an angle of 45° to the normal axis of the target surface on its front side (see Fig. 1) and consisted of a stack of alternating filters and IPs of MS-type housed in a thick lead shield (Fig. 3). The distance from the target chamber center (TCC) was 220 mm. Each IP recorded the temporally, spatially, and frequency integrated signal of the hard x rays emitted from the target and propagated through the filters in front of it. These x rays are mostly bremsstrahlung emission generated by HEs colliding with atoms and ions in the target. The x-ray signal was gradually attenuated by each filter so that progressive IPs inside the BSC recorded the contribution of higher-energy portions because of the filtering out of lower-energy photons. Thus, the instrument recorded photons with energy greater than 10 keV, thereby excluding the copper K_α signal. Furthermore, electrons up to ~1 MeV were prevented from penetrating the stack thanks to several PTFE (C_2F_4) filters placed at the entrance. The IPs were scanned successively with a Fuji Image Reader BAS-1800, and the photostimulated luminescence (PSL) signal over each IP and the relative error were extracted from the scanned files; the PSL values are related to the dose deposited according to calibration curves obtained in

Ref. 39, and the uncertainty related to this signal is determined by the noise level measured in the region of interest. An example of the signal measured in the IP stack is shown in Figs. 3(b) and 3(c). Labeled as 1 in Fig. 3, the first IP corresponds to the signal filtered by the first Al layer and was discarded to avoid the possible effects of plasma emission. The color scheme in Fig. 3(b) shows the decrease of signal intensity measured by the progressive IPs.

Tentori et al.[34] described in detail the post-processing techniques used for the signal obtained by the BSC. Briefly, the parameters for the HE distribution and thus the resulting photon spectrum can be found by comparing the signals measured on the IPs with synthetic signals generated by GEANT4 simulations. The procedure involves calculating the detector response (which is done with multiple GEANT4 runs) by injecting monoenergetic photons into the synthetic diagnostic; the spectral response for each photon energy consists of the energy absorbed by each IP per photon in the simulation. The photon spectrum detected by the diagnostic is assumed to be described by a function of the form $f_{ph}(E) = A/E \cdot \exp(-E/T_{ph})$, with the values of the parameters A and T_{ph} retrieved by performing chi-square analysis against the experimental signal, as explained by Tentori et al.[34]

By applying a similar method, starting from the x-ray spectrum retrieved with the procedure described above, we reconstructed the energy distribution of HEs originating from the x rays by the bremsstrahlung process while propagating into the target. For this purpose, GEANT4 simulation runs were performed, with monoenergetic electrons with variable energy injected into the multilayer target in the direction of the laser and a simulated detector placed
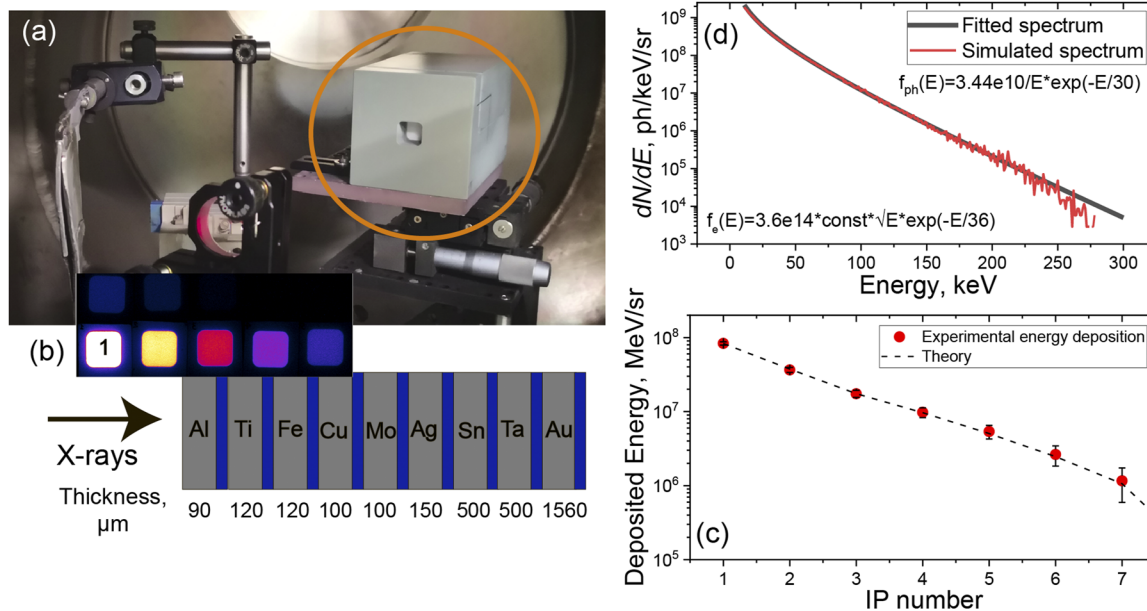

FIG. 3. (a) Hard x-ray spectroscopy setup inside vacuum chamber using bremsstrahlung cannon (BSC). (b) Materials and thicknesses of progressive filters for signals measured in imaging plates (IPs); not shown here are the PTFE (C_2F_4) filters used to stop electrons from penetrating the stack. (c) Measured dose as function of channel number, and comparison to dose fitted from model. (d) Comparison between x-ray spectrum $f_{ph}(E)$ (black line) fitting signals in (b) and bremsstrahlung spectrum produced by 3D Maxwellian distribution of electrons $f_e(E)$ (red line) propagating through target. The photon and electron distributions calculated by GEANT4 have temperatures of 30 and 36 keV, respectively.

where the BSC would be in relation to the target and laser. With the response from each set of electrons recorded individually, the HE source corresponding to any arbitrary x-ray spectral distribution could be retrieved, and this allowed also to simulate the effect of the target composition on the measured x-ray spectrum. To compare the synthetic signals with the experimental ones, a chi-square minimization method was used to optimize the parameters of the fitting procedure. Assuming a single-temperature 3D Maxwellian distribution for HE energy $f_e(E) = 2/\sqrt{\pi} \cdot A/T_e^{3/2} \cdot \sqrt{E} \cdot \exp(-E/T_e)$, the HE temperature ($T_e$), absolute number of electrons (A), and their total energy could be calculated for each laser shot. As an example, the photon and electron distributions obtained for shot 55 196 (a target with a carbon ablation layer) are shown in Fig. 3(c).

C. Electron magnetic spectrometers

Three identical ESs were placed in front of and behind the target, allowing us to directly measure the energy distribution of the electrons departing from the TCC in the backward direction (ES1 and ES2) and accelerated in the forward direction and exiting the target (ES3). They were installed in the vacuum chamber on a breadboard in the horizontal plane at angles of 25° (ES1), 51° (ES2), and 31° (ES3) with respect to the normal to the target, as shown in Fig. 4. The ESs were based on magnetic deflection[27] and consisted of a 1 mm beam collimator, ferrite magnets with a field of 80 mT, an IP holder, and a shielding case. They allowed us to measure the energy spectrum of the electrons from 50 keV to 1.5 MeV. The low-energy cutoff was produced by a gap between the entrance hole and the IP, so that less-energetic electrons were deflected in the magnetic field toward the ES front shield and could not hit the IP. The distance to the TCC was 300 mm for each ES, resulting in a solid angle of HE measurement of 9×10^{-6} sr. The calibration of the position on the IP (determined by the deflection angle) and the electron energy was obtained using particle tracking simulations.[27] These parameters allowed an accurate angular scanning of electron emission from typical laser-induced plasmas at PALS. With the method of alignment that was used, the accuracy of the electron spectrometer

alignment was less than 1 mrad. See Krupka *et al.*[27] for more details about the ESs that were used.

The electron spectra retrieved from the scanned IPs show a clear exponential decreasing trend in the range of energies from 150 keV to 300–450 keV (Fig. 4), depending on the shot. The portions of the spectra at lower and higher energies are not considered here because of the effects of magnetic and electric fields on the trajectories and the critical correction for the IP efficiency and noise, respectively. For the analysis, we therefore fitted the spectra in the energy range of 150–300 keV by using a 3D Maxwell function as done for the BSC data. For ES1 and ES2, the HE source is described satisfactorily by the temperature of the Maxwellian distribution fitting the spectrum, while the spectrum measured by ES3 is significantly different from the spectrum of HEs entering the target, this being because of the effects of HE propagation. A direct comparison of the ES3 spectra measured for different targets is also complicated by the different Z values of the ablators, resulting in a different stopping power and a different efficiency of bremsstrahlung emission. Here, the effects of HE propagation into the target on the measured spectra were estimated by using dedicated GEANT4 simulations, as discussed below.

D. X-ray spectrometer

A focusing spectrometer with spatial resolution (FSSR) was also placed in the vacuum chamber for some laser shots to measure the ratio between bremsstrahlung and K_α emission for each ablator. It was based on a spherically bent crystal of quartz (2243) with $2d = 2.024$ Å and a radius of curvature of $R = 150$ mm, measuring characteristic x-ray lines in the spectral range of $\lambda = 1.38–1.56$ Å. The spectrometer observed the K-shell line emission at an angle of 50° from the front target surface with a demagnification of 0.41. The emission was registered on an IP and scanned with an Amersham Typhoon IP scanner (equivalent to GE 7000). The detector holder was covered with aluminized polypropylene foil (1 μm CH$_2$ + 0.2 μm Al) to protect the IPs from optical radiation and with 10 μm-thick Cu foil to suppress the spectral background. The
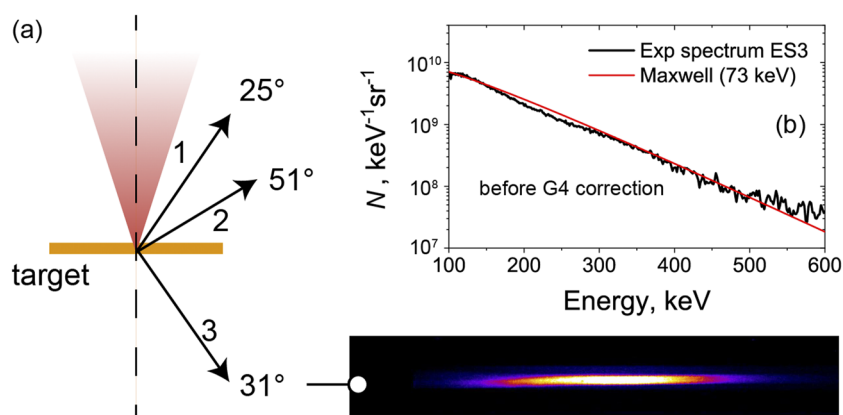

FIG. 4. (a) Experimental arrangement of hot electron (HE) spectrometers. The angles 25° (ES1), 51° (ES2), and 31° (rear, ES3) are with respect to the target normal. (b) Typical electron spectrum measured by spectrometer ES3, and Maxwellian function fitting the experimental data. The experimental spectrum is not corrected for the electron propagation through the target.
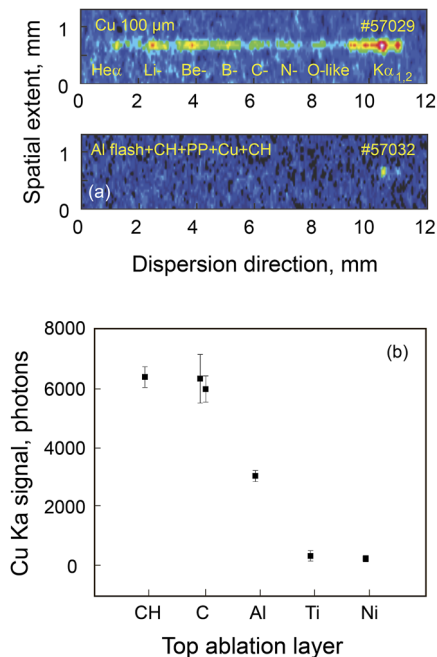
FIG. 5. (a) Spectra of Cu K_α group recorded in shots irradiating Cu foil (top) and composite target with Al flash + CH ablative layer (bottom). The absence of the K-shell emission from highly ionized Cu indicates a relatively low temperature of the buried diagnostic layer. (b) Temporally and spatially integrated Cu $K_{\alpha 1}$ signal collected on IP and emitted from different types of composite targets. For Ti and Ni ablators, the K_α emission cannot be extracted unambiguously from the spectral background.

crystal was protected by 13 μm-thick kapton foil. Figure 5(a) shows two experimental spectra obtained from laser shots on Cu foil and a multilayer target, while Fig. 5(b) shows the measured values of the Cu $K_{\alpha 1}$ signal emitted from different composite targets. The absence of highly ionized states for Cu K-shell emission in the case of multilayer targets implies low plasma temperatures[29] as considered in Fig. 2(b).

E. Hydrodynamic simulations

To retrieve the evolutions of the plasma density scale length and coronal temperature, the interaction conditions were simulated using the radiative-hydrodynamic code CHIC,[18] in a way similar to that described by Cristoforetti *et al.*[22] These parameters play a primary role in determining the intensity and the energy distribution of the laser-driven HE beam. In particular, in the CHIC code, HE generation is implemented[40] by using appropriate scaling laws and local and instantaneous values of laser intensity and plasma parameters. The HE generation is simulated here by accounting for the interplay between two-plasmon decay (TPD)/stimulated Raman scattering (SRS) and the hydrodynamics of the plasma. The plasma temperature in the CHIC simulation shows a peak value in correspondence with the laser peak, increasing from 3 to 5.5 keV with the atomic number Z of the materials. The density scale length increases with time and shows no significant differences among the materials

(the maximum difference is ~10%), being ~90–100 μm at the laser peak time (150–160 μm at +200 ps).

III. DATA ANALYSIS AND DISCUSSION

The aim of the present paper is to validate existing models and results of HE generation by comparing different but complementary diagnostics for characterizing HEs in ICF experiments, highlighting the capabilities and disadvantages of each of them. In what follows, we discuss several issues in light of the present results, including the determination of HE temperature, amount, divergence, and time evolution.

A. Hot-electron temperature

As described above, the temperature T_e of the HEs produced by LPI can be estimated by using both the ES and BSC data. We are particularly interested here in the HEs propagating in the forward direction inside the target, which are the more-critical ones for ICF. Figure 6(a) shows the values of T_e obtained from the BSC x-ray spectra for all the target types and for laser intensities in the range of $(0.3–1.2) \times 10^{16}$ W/cm^2; as can be seen, T_e tends to increase with increasing laser intensity, with no evident dependence on the ablator composition. The electron temperatures measured by BSC and ES3 are compared in Figs. 6(b) and 6(d); for an appropriate comparison, we use the data of spectrometer ES3 because it records the forward-propagating HEs as those producing the hard x rays measured by the BSC, while spectrometers ES1 and ES2 record backward-propagating electrons. We also assume that ES3 and BSC measure the same population of HEs, this being because the x rays from deep target layers are less energetic and are attenuated by propagation in the target, especially in the Cu layer or in the high-Z ablator. The black dashed line in Figs. 6(b) and 6(d) indicates the ideal case when the temperatures measured by the two diagnostics are equal. The errors in the electron temperature measurement (not shown in the figure for clarity) were typically ~3–7 keV for both diagnostics. As can be seen, the temperatures calculated by fitting the raw spectra measured by ES3 are always higher than those estimated by the BSC data. The larger discrepancy is observed for targets which used a higher-Z ablator, i.e., Ti and Ni; this suggests that populations measured by ES3 are likely to be impacted by their propagation through the target.

GEANT4 simulations similar to those described above for analyzing the BSC data were used to estimate the effect of the transport of HEs into the target on their energy distribution. Monoenergetic electrons were injected into the target, and a synthetic detector was placed at the corresponding location of ES3 in the experiment. The expected spectrum of electrons recorded by ES3 can be estimated for any arbitrary distribution of electrons launched into the target. Note that a cold and unexpanded target is assumed here because the code accounts for neither the target ionization nor the hydrodynamic expansion of the ablated layer; however, these approximations are not expected to change the electron propagation significantly.[41,42] In fact, simulations of deposited energy[41,42] in our range of 150–300 keV showed that the discrepancy between a heated target and a cold one is less than 10%. GEANT4 simulations also account for neither plasma effects into the target nor the effect of the sheath field produced on the rear side of the target;
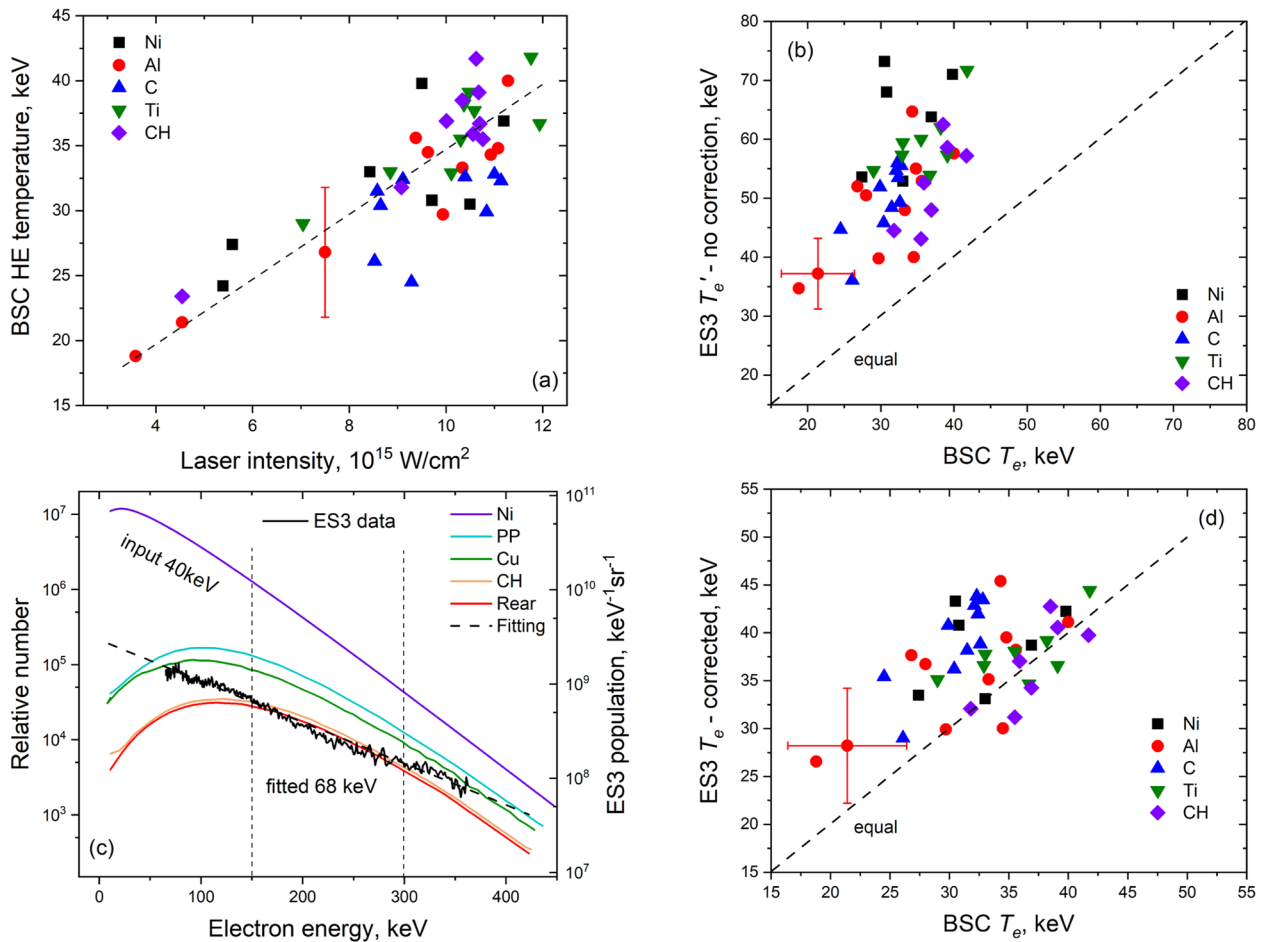
FIG. 6. (a) Electron temperatures measured by BSC diagnostics vs laser intensity. For better readability, a typical error bar is given for only one of the points. (b) and (d) Comparison of electron temperatures estimated from BSC x-ray spectra with those obtained from ES3 spectrometer before (b) and after (d) the GEANT4 correction accounting for transport into the target (d). The electron spectra were recorded behind the rear side of the target, and the dashed lines indicate equal values for the BSC and ES3 diagnostics. (c) Modification of energy distribution of HEs along their propagation into a multilayer target with Ni ablator, obtained from GEANT4 simulations. The violet curve is the 3D Maxwellian distribution of HEs with temperature 40 keV injected into the Ni ablator; the other curves are the distributions expected at different target layer interfaces. The red curve is the electron distribution at the rear side of the target, and it is fitted by an exponential function with a temperature of 68 keV (black dashed line) in the energy range of 150–300 keV. The experimental electron spectrum for shot 55 189 (black solid line) measured by the ES3 spectrometer is overplotted in the graph, suggesting that the measured spectrum with a temperature of T'_e = 68 keV corresponds to an input HE population with a temperature of T_e = 40 keV.

the latter results in a significant refluxing[43] of low-energy electrons that cannot overcome the potential barrier and a reduction of the energy of the electrons that can leave the target. By assuming that the energy cutoff produced by the sheath field is of the order of the HE temperature,[44] we estimate that the sheath field should not significantly affect the spectrum in the high-energy tail used for the analysis ($E_{HE} > 100$–150 keV).

Figure 6(c) shows clearly how collisions of HEs into the target affect their energy distribution, where a Maxwellian HE distribution with T_e = 40 keV is injected into the target with a Ni ablator (purple curve); the other colored curves represent the distributions of electrons reaching the different layers in the target, with the red curve being the expected distribution of electrons escaping from the rear side. Note that the population of HEs measured at the rear target

surface in the energy range of 150–300 keV is one to two orders of magnitude lower than the original injected population. Mimicking the analysis of the experimental data, an exponential fit of the red curve in the range of 150–300 keV results in a temperature of 68 keV, i.e., 1.7× higher than the temperature of the injected electrons. This shows the need for post-processing the experimental spectra by accounting for the collisions simulated with GEANT4 to estimate the temperature of the HEs before entering the target. The results of this procedure are shown in Fig. 6(d), where the values of T_e obtained from the BSC x-ray spectra are compared with those obtained from the ES3 spectrometer after the above correction. The points now lie much closer to the dashed line, suggesting that it is collisions that dominate the deviation of the ES3-measured spectrum from that generated at the TCC.

The HE temperatures measured for the forward-propagating HEs agree with those from previous experiments[22,45,46] and particle-in-cell simulations[47] under similar irradiation conditions, and they can be explained by electron acceleration in plasma waves driven by parametric instabilities. In particular, the HE temperatures agree with the phase velocities of plasma waves driven by convective SRS or TPD in the underdense plasma.[48]

The temperature of electrons obtained by the spectrometers located in front of the target (ES1 and ES2) is noticeably different from that obtained by the rear spectrometer ES3. The discrepancy is particularly striking for the data obtained by ES1 installed at 25°, giving usually higher values of electron temperature up to 70–80 keV. An additional difference between the data of the front and rear spectrometers is the energy distribution of the HEs; in fact, for a considerable amount of shots, the front HE spectra have a clear additional spectral component that peaks in the range of 300–500 keV [see Fig. 7(a)]. The evident differences between the electron distributions and temperatures obtained by the front and rear spectrometers can be explained by the different generation mechanisms and the effect of the strong azimuthal magnetic field in the spectra measured in the front side.

The values of electron temperature obtained by fitting the ES1 data in the range of 150–250/300 keV are consistent with the Beg scaling,[49] giving $T_e \approx 70$ keV for a laser intensity of 2×10^{16} W/cm^2. This agreement suggests that the main contribution of backward-propagating HEs is from electrons accelerated by resonance absorption (RA) at the critical density,[50] which is made possible by the

rippling of the critical density surface or by the low $f/\#$ number of the laser focusing system. In fact, simulations suggest that these electrons propagate from high-density to underdense plasma along the density gradient[51] and therefore could be partially measured by ES1. Note that our results correspond to the lower limit of Beg scaling mentioned by Beg *et al.*[49] and have a linear dependence in this range.

The high energy peak (300–500 keV) observed in some HE spectra [Fig. 7(a)] suggests that an additional mechanism is at play for the generation of backward-propagating HEs, but its origin is unclear. The presence of additional peaks in the electron spectra in the range of 250–400 keV could perhaps be explained by Pukhov scaling,[52] which gives $T_e > 200$ keV for our parameters. Although the scaling applies to different intensities and time scales, the presence of a long-duration intense laser can produce sufficient quasi-stationary electric and magnetic fields in the plasma.[53–55] Moreover, the presence of laser speckles is expected to result in local values of laser intensity that are much higher than the nominal value of the laser envelope.[4,56] In the context of laser plasma accelerators, peaks in the electron spectra are related to the localized injections of electrons into the accelerating plasma wake.[57] However, the situation here is different because electron plasma waves are excited by RA, TPD, and SRS[11] rather than by laser wakefield acceleration and are unable to produce almost-monochromatic HE bursts at such high energies, so further experiments are needed to investigate the related acceleration mechanism.

B. Hot-electron conversion efficiency

Here, we discuss the experimental data obtained by the different diagnostics in order to assess their capability to provide information about the absolute and relative amounts of HEs propagating through the target.

In Fig. 7(b), we plot the absolute number of electrons per solid angle obtained for all the shots from analyzing the ES3 and BSC data. The plotted values are the population parameters of the Maxwellian distribution obtained by the best fitting of the experimental data, and they can be equated with the recorded doses because the electron temperatures of BSC and ES3 are equal as shown in Fig. 6(d). The amount of HEs obtained from the ES3 data accounts for the different stopping powers of the ablators, which were calculated by GEANT4. The corresponding transmissivity of a Maxwellian electron distribution through the different targets is shown in Fig. 8(a) for various HE temperatures. These curves were obtained by injecting electrons at a distance of 200 μm from the target surface with a spot size of 50 μm and a cone angle of 45°. The electrons were distributed into 45 energy bins spaced logarithmically from 10 keV to 2 MeV, then the transmitted electrons were acquired by a synthetic diagnostic taking into account the position and solid angle of the spectrometer in the real experiment. Finally, the transmissivity was calculated by considering the total population of the Maxwellian distribution.

Figure 7(b) clearly shows that the amount of HEs retrieved by ES3 is always lower than that calculated by the BSC diagnostics. A possible cause of this discrepancy is a lower divergence of the HE source as suggested by the analysis of K_α imager data (see below); this could result in an underestimation of the amount of HEs detected by ES3, which is located at 31° from the target normal.
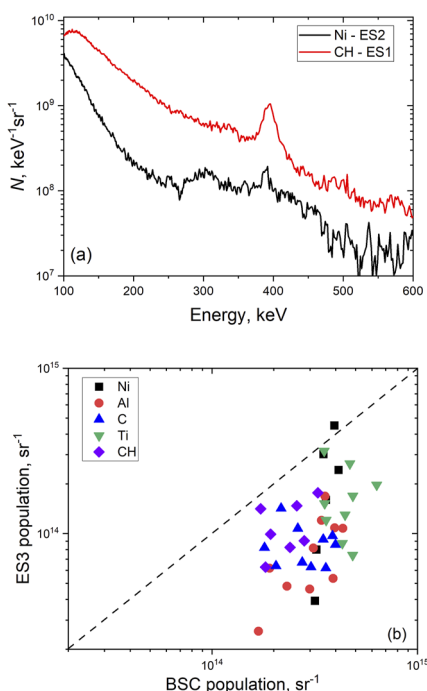

FIG. 7. (a) Examples of electron spectra for shots with Ni (high *Z*) and CH (low *Z*) ablation layers from front spectrometers. (b) Comparison of HE source populations registered by BSC and ES diagnostics. The dashed line corresponds to equal populations, and the ES data account for transmission through the target.
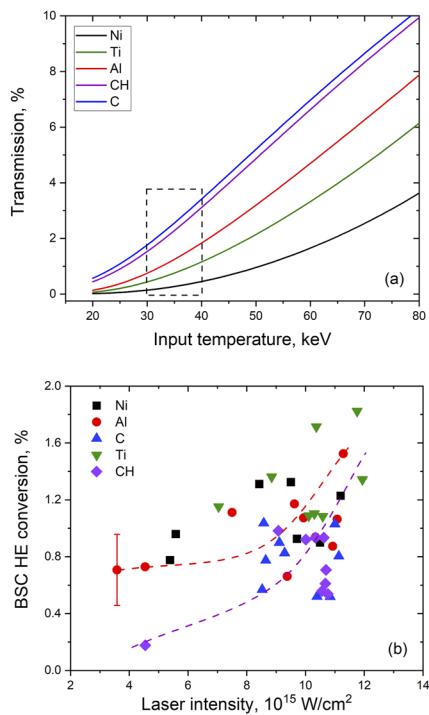
FIG. 8. (a) Calculated transmission of HEs emerging from rear surface of target as estimated by GEANT4 simulations. The values were calculated by injecting Maxwellian distributions of electrons with different input temperatures on the front surface of the target. Electrons were injected at 200 μm from the target surface with a spot size of 50 μm and a cone angle of 45°. The dashed rectangle shows the typical range of measured electron temperatures in the experiment. (b) Conversion efficiency of laser energy into HE energy obtained from analyzing BSC data. The dashed lines are to guide the eye and emphasize the trends for Al and parylene-C ablators, whereas the actual dependence can be different. For clarity, a typical error bar is given for only one of the data points.

This is also confirmed by the GEANT4 simulations, in which the transmission of HEs through the target material depends strongly on the cone angle, the spot size, and the energy range of the spectrum. Therefore, the strong dependence of the results on the HE propagation direction makes the HE spectrometers unsuitable for obtaining an accurate estimation of the HE amount.

On the other hand, a dedicated set of GEANT4 simulations revealed that the HE information retrieved from BSC data is affected only slightly by the HE divergence when the acquisition geometry is accounted for. Therefore, BSC data allow one to obtain a more reliable estimate of the total energy of HEs and then of the conversion efficiency of laser energy into HEs. The values of the conversion efficiency of laser energy into HEs obtained from analyzing BSC data are shown in Fig. 8(b) for all the laser shots. Most of the values are between 0.5% and 1.5%, similar to those obtained in other SI-relevant experiments (such as at the Omega Facility[58] or NIF[59]). No clear dependence of conversion efficiency on the ablation layer is observed, except for a distinctly lower conversion efficiency in the case of parylene-C and carbon (i.e., low Z) targets. For each ablator, the graph also shows an increasing trend of conversion efficiency

with laser intensity. These values can be compared with those provided by CHIC simulations accounting for SRS and TPD scaling as given by Antonelli *et al.*[60] and performed under the same laser conditions. The latter gives conversion efficiencies of HEs driven by SRS and TPD of 2.3% and 1.1%, respectively, and HE temperatures of the two populations of 39 and 93 keV, respectively. The values corresponding to HEs accelerated by SRS plasma waves are closer to those measured by BSC and ES3 (see above), although the conversion efficiency is twice as high. Note here that our conversion efficiencies given in Fig. 8(b) refer only to HEs propagating in the forward direction because the HE populations measured by ES3 and BSC are very similar [see Fig. 7(b)].

HEs propagating through the target undergo multiple collisions with free and bound electrons, resulting in both bremsstrahlung continuum and bound–bound line emissions. The K_α imager measures the intensity of the 2p $\longrightarrow$ 1s fluorescence driven by the collisions of HEs with K-shell electrons in the Cu tracer layer. Therefore, this diagnostic provides indirect information—time-resolved here—about the total amount and spatial distribution of the HEs. However, the signal from the imager is usually integrated over a narrow spectral bandwidth determined by the size of the crystal, which is here less than 1.4 mÅ. Spectral integration does not allow one to distinguish the relative contribution of the signal originating from the K_α line and that due to the plasma corona continuum emission under the line; consequently, the prevailing contribution of the emission is *a priori* unknown and deserves more-detailed investigation, analogous to studies of HE effects in laser-irradiated bare Cu targets.[29]

To disentangle the two contributions, in a limited number of shots we measured the x-ray spectrum in the range $\lambda = 1.38$–1.56 Å by using an x-ray spectrometer (see Sec. II). The spectrum obtained for the target with a parylene-C ablation layer is reported in Fig. 5(a), showing that the K_α emission line is more intense than the continuum background emission in the same spectral range. A distinct K_α emission above the continuum was also observed for targets with C and Al ablators. Typically, the recorded ratio of $K_{\alpha1}$ maximum vs bremsstrahlung emissions was greater than 2.5 for all these targets, except for shots with low laser energy. This implies that the spectrally integrated signal measured by the K_α imaging system is dominated by K_α emission, and therefore this diagnostic can be safely used as marker of HEs. However, low-energy shots were excluded from the following analysis because of the lower $K_{\alpha1}$ intensity. On the other hand, in the x-ray spectra obtained by using targets with high-Z ablators (Ti and Ni), the K_α emission is very faint compared to the bremsstrahlung and plasma coronal emission, implying that K_α imaging diagnostics cannot be used for those shots.

This scenario was also confirmed by using FLYCHK[61] and GEANT4 simulations, as shown in Fig. 9(a). In the graph, we compare the expected number of photons detected by the K_α imager, which are produced by (i) K_α fluorescence due to HE collisions in the Cu layer (green curves), (ii) bremsstrahlung emission due to collisions of HEs into the target (blue curve), and finally (iii) emission from the coronal plasma in front of the target due to bremsstrahlung and recombination processes (red and black curves). The values for (i) and (ii) were simulated by using GEANT4 and considering a Maxwellian HE distribution with a temperature of 40 keV [Fig. 6(a)] and a total energy of 3 J, as obtained by the BSC diagnostics. Note that the simulation of the K_α emission in GEANT4
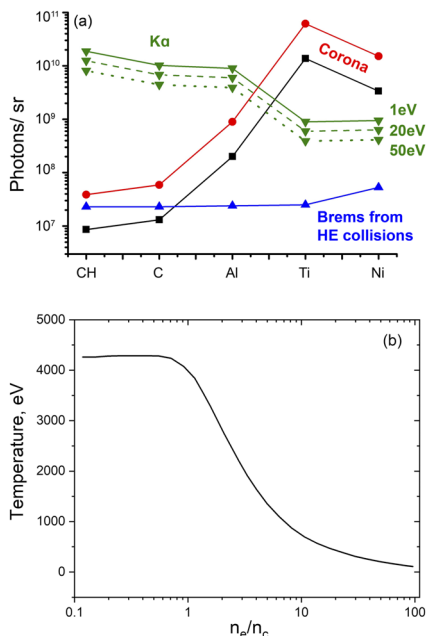
FIG. 9. (a) Number of $K_{\alpha 1}$ photons (green) for different values of Cu layer (solid, dashed, and dotted lines) measured by K_α imager, compared to number of bremsstrahlung photons produced by collisions of HEs into target (blue line) and to the number of bremsstrahlung + recombination photons emitted by the plasma corona, calculated in 1D (black) and 3D geometry (red). The first two values were estimated by using GEANT4 simulations and the last one by post-processing the results of hydrodynamic simulations with the FLYCHK code. (b) Typical plasma conditions along density profile, derived from CHIC hydrodynamic simulations, and successively post-processed in the FLYCHK simulations. The plot corresponds to the conditions at the time of laser peak arrival on the Al ablator.

the radiation. The same procedure was repeated at different times along the laser pulse, integrating the emission at discrete temporal intervals. Figure 9(b) shows only the plot corresponding to the conditions at the time of laser peak arrival on the Al ablator, while other temporal profiles were simulated with a step of 100 ps. The values shown in Fig. 9(a) confirm that K_α line emission is overcome by coronal emission for high-Z ablators such as Ni and Ti. This means that the K_α imager data are only acceptable for targets with low-Z ablation layers, and therefore other cases were subsequently ignored.

The typical conversion efficiency of HE energy into Cu $K_{\alpha 1}$ photons estimated by the Cu K_α imager was less than 0.1% and was slightly higher for Al multilayer targets if compared to that obtained for C and parylene-C ablation layers. We observe that the photon yield for all the targets is correlated well with the HE population given by ES3 [see Fig. 10(a)]. However, despite being correlated well, the data for Al targets are shifted with respect to those for C and CH targets because of both the stopping power in the target and the different heating of the Cu tracer layer.

The above analysis suggests that care should be taken when estimating the HE flux via K_α imaging. In fact, a rigorous approach to this quantification requires detailed hydrodynamic and Monte Carlo/numerical modeling to assess the contribution to the signal due to continuum x-ray emission (including the corona or HE bremsstrahlung emission) and the percentage of the K_α line profile (widened by the target heating) effectively measured by the imager
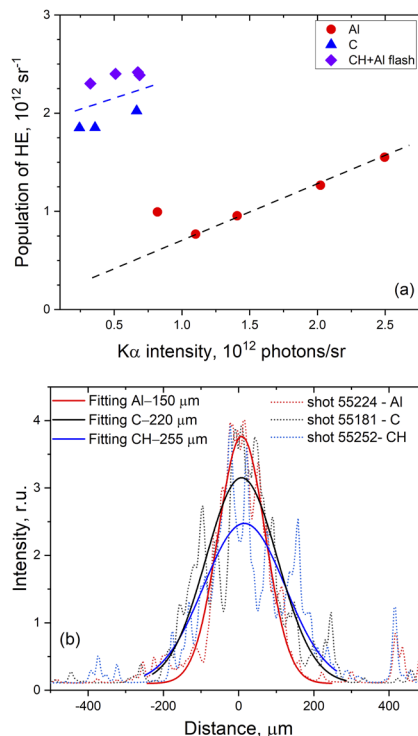

FIG. 10. (a) Dependence of HE population registered by rear electron spectrometer in range of 150–300 keV on K_α intensity. (b) Spatial FWHM profiles of K_α emission registered by K_α imager for different targets used in experiment.

is quite crude and based on the libraries of PENELOPE[62] and/or Livermore[63] for experimental and theoretical effective cross sections for inner shell ionization by electron impact in a cold material. In particular, the broadening of the spectral lines and frequency shift are not accounted for. In [Fig. 9(a)], the number of K_α photons was therefore corrected by accounting for the effective portion of the line acquired by the imager for different electron temperatures of the tracer layer [see the dashed and dotted lines in Fig. 9(a)] using the line profiles simulated by FLYCHK in Fig. 2(b).

Coronal emission (iii) is simulated by post-processing the plasma conditions given by the CHIC hydrodynamic code with the collisional radiative FLYCHK code. First, we considered a 1D plasma approximation (black solid line) and calculated the photon emission relying on the longitudinal profiles of density [Fig. 9(b)] and temperature along the central axis. Next, we estimated the correction due to the 3D geometry (red solid line) of the plasma by considering a 3D plasma hemisphere. The coronal emission was obtained by integrating the emissivity in different regions of the plasma density profile by considering discrete bins centered at densities from $0.1n_c$ to $60n_c$. For all the ablators, the emissivity in each region was determined by using FLYCHK at the density and temperature values given by the hydrosimulations. The total emission was determined by summing the contributions of all the regions, neglecting the reabsorption of

as discussed for example by Renner *et al.*[29] Some of these issues might in principle be overcome by using a K_α spectrometer, which can directly quantify the background below the line and exclude uncertainties due to the line shift and width. On the other hand, the collection efficiency of the imager is considerably higher than that of the spectrometer, so choosing the optimum experimental strategy is not completely straightforward.

C. Divergence and time evolution of hot electrons

In the geometric scheme used for the K_α imager, because of the quasi-monochromacy of the imager spectral window, the horizontal size of the signal in the streaked image [Fig. 2(a)] depends only on the size of the source (and on instrumental functions of the crystal used, which have been taken into account) and not on the full spectral distribution of the emitted x-ray radiation. This makes this diagnostics the most suitable for investigating the spatial distribution and the divergence of the HEs.

Typical spatial profiles of the K_α emitting regions obtained in shots with CH, C, and Al ablators are shown in Fig. 10(b), where the curves were obtained by a vertical integration of the streaked images over the full temporal sweep. As can be seen, the K_α extent obtained in shots on Al ablators is usually smaller than that obtained on CH and C targets. By considering the available set of shots, the average value of the K_α widths for Al targets is 170 ± 15 μm, and those for CH and C targets are 240 ± 50 and 250 ± 20 μm, respectively, where the second number is the standard deviation and therefore represents the shot-to-shot reproducibility. The spread of the observed values was higher for the CH ablator, going from 170 up to 310 μm, while carbon and aluminum ablators showed more-stable values. The HE extent can be used to evaluate the divergence of the HEs penetrating the target. For this issue, we need an assumption about where the HEs are generated with respect to the target surface. Here, we assume that HEs are generated within an area comparable to the focal spot size (FWHM = 100 μm) and are driven by SRS or TPD in the density range of $0.15n_c$ to $0.25n_c$. This assumption agrees with the experimental observation of SRS spectra from PALS experiments, e.g., in Ref. 64. Consequently, the position of the HE source can be determined by considering the density profiles given by hydrodynamic simulations at times of K_α emission. By using these values, we obtained a divergence of $\pm 25°$ for C and CH targets and a much lower value of $\pm 10°$ for Al targets. Our measurements of the HE divergence are consistent with the results given in Ref. 65, where a more planar (axial) expansion enforced by a heavier plasma was observed. These values suggest that the HE spectrometer (which detects forward-accelerated electrons) should be placed in this angular range for optimal detection. Therefore, in the current measurements, the ES3 spectrometer tended to underestimate the HEs generated in shots with Al ablators, which have smaller divergence. However, note that the measured spatial extent of K_α (and hence the estimated divergence) can be affected by a possible angular dependence of HE energy, as shown in some experiments and kinetic simulations.[43] In our experiment, in fact, only energetic electrons ($E_{HE} > 55$ keV for parylene N and $E_{HE} > 75$ keV for aluminum multilayer targets) can reach the Cu tracer layer. Therefore, the divergence of lower-energy electrons can differ from that estimated above. Also, the comparison between the K_α extent and divergence in different targets can be affected by the different

stopping powers of the ablators. The sheath effect from the rear side of the target can in principle lead to an incorrect determination of the divergence of the HEs, but our design of the target minimizes this effect because the last parylene-N layer absorbs most of electrons reflected back to the copper tracer.

The typical duration (FWHM) of K_α emission was 250–300 ps for laser intensities of the order of 10^{16} W/cm^2 [Fig. 11(a)], which is slightly shorter than the duration of the laser pulse (300–370 ps). The mean duration measured for the carbon and parylene-N ablators was less than that for the aluminum one [Fig. 11(a)]. At lower laser intensity, we measured a longer K_α duration in the case of the aluminum ablator, and this effect could be related to the spectral shift of K_α discussed in Fig. 2(b). In fact, a higher laser intensity could produce a faster and higher heating of the target and of the Cu layer, and therefore a faster and larger shift of the K_α line out of the spectral window. This mechanism could in principle affect also the comparison of temporal durations obtained for different targets because of the different conversion efficiencies of HEs and the different stopping powers of the targets. More experimental and/or numerical investigations are therefore needed to quantify the extent of this phenomenon.

The absolute temporal calibration of the XRS allowed us to measure the timing of the K_α emission with respect to the laser maximum, as shown in Fig. 11(b), and the uncertainty of the time of K_α emission is estimated to be ± 45 ps.[37] The timing of HE generation depends on the time needed to establish the optimal conditions in the plasma (e.g., density scale length and temperature) for the
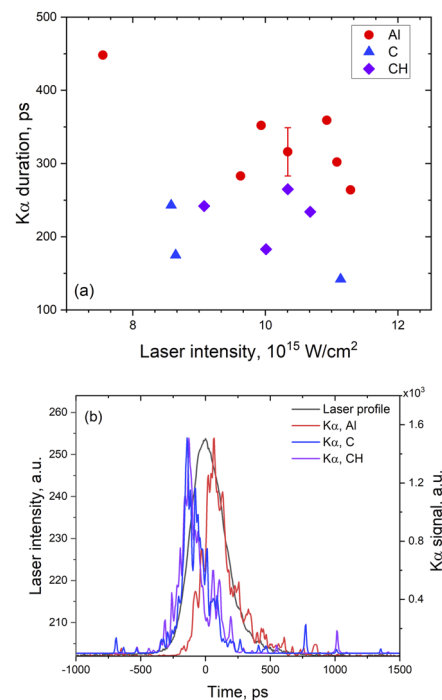

FIG. 11. (a) Dependence of K_α emission duration on laser intensity for different target ablators. (b) Timing of HE generation as measured by K_α emission vs laser pulse profile observed in shots over CH, C, and Al ablators.

development of parametric instabilities at the given laser intensity. When combined with a time-resolved diagnostic of parametric instabilities driven in LPI, this information can contribute to unequivocal identification of the mechanism responsible for HE generation under ICF conditions.[8,66] In addition, in a full-scale SI scenario, the time of HE generation influences the preheating of the fuel. In the present experiment, the delay of maximum HE generation with respect to the laser peak Δt_{HE} was larger for the Al ablation layer ($\Delta t_{HE} \approx 20$ ps), while the C and CH ablators typically displayed negative values ($\Delta t_{HE} \approx -70$ ps), implying that HEs are mainly generated before the laser maximum. Note that the different timings of HE bursts between the aluminum and carbon/parylene-N data could be affected by a possible spectral shift of the generated K_α line. In fact, aluminum ablators absorb more energy from HEs, resulting in fewer HEs reaching the Cu tracer layer and therefore a lower heating of Cu; consequently, we expect that the shift of the K_α line outside the spectral window is smaller for Al ablators, allowing one to observe the emission at later times. However, a detailed interpretation of these effects requires further dedicated experiments. See elsewhere for more details about the measured delays and their relationship to ICF.[32,37] A detailed spectroscopic and calorimetric analysis of backscattered light combined with the HE characterization[22,32] suggests that SRS instabilities could be the predominant mechanism producing HEs. The reasons for HE quenching after the laser peaks are still not clear and deserve new investigations, but an LPI investigation (not shown here) suggested that both TPD and SRS are also driven before the laser peak and that SRS reflectivity seems to correlate better than TPD with the K_α time profile.

D. Comparison with other SI-relevant experiments

Our experimental results were compared with previous measurements and simulations performed at the PALS facility by our and other groups.[10,11,22,29,43,60,65,67,68] Note that the density scale length and plasma coronal temperature reached under these conditions are typically lower than those envisaged in a full SI experiment.[59,69] Different schemes were used for these experiments: in some experiments, the targets were massive and too opaque for HEs to be observed from the rear side, while other targets were composed of plastic ablators (tens of micrometers thick) on which the laser was focused, followed by mid-Z tracers (usually copper or titanium). Note that multilayer targets are also very useful for providing information about hydrodynamic and HE effects when using a shock breakout technique.[60]

Table I summarizes the key experimental parameters used in experiments performed in past decades at the PALS facility at 1ω, showing the results obtained under similar interaction conditions. In particular, the HE temperature T_h (assuming a Maxwellian distribution) and the laser-to-HE energy conversion efficiencies are reported for each experiment. Unfortunately, it is not always noted what type of Maxwellian distribution (2D or 3D) was used to infer the HE temperature, so measurement uncertainties of up to 20% are possible during the comparison. We also found that only Antonelli et al.[60] and Cristoforetti et al.[22] considered a two-temperature distribution function to interpret the experimental data. Therefore, we distinguish the results obtained for massive and multilayer targets because they usually consider different HE populations.

The experiments with massive targets[10,43,65,68] involved self-generated spontaneous magnetic fields and measuring HEs from the front side of the target because of the RA mechanism. Our electron temperatures measured by front electron spectrometers (i.e., for HEs propagating backward) are consistent with those cited above. For all experiments with multilayer targets (including ours), we observe T_h values of ~30 keV (measured from the rear side of the target and by BSC, i.e., for HEs propagating forward). The conversion efficiency reported by Antonelli et al.[60] and Cristoforetti et al.[22] slightly exceeds our measured values, but it was based on the K-shell time-integrated emission and so it is important to note that it measures the Cu atoms' response to HEs with energies above the K-edge (or ionization) limit, which is close to 9 keV. By contrast, Renner et al.[29] showed the minimum conversion efficiency. The limited range of photon energies and the complicated calculation scheme in the numerical model are possible reasons for the different values. For comparison, the conversion efficiency given by Batani et al.[11] is based on a similar method but is significantly higher.

In our experiment, the measured population of backward-propagating HEs was sufficiently lower than that of forward-propagating ones. This result validates the conclusion presented in

TABLE I. Summary of shock ignition (SI)-relevant experiments performed at PALS facility at 1ω, i.e., at $\lambda = 1315$ nm. The target configuration and the key laser parameters used in each experiment are reported. In particular, we indicate the total laser energy E_{tot} delivered on target and the laser intensity I. The measured HE temperature T_h and the laser-to-HE energy conversion efficiency η are reported in the last two columns. If a paper considers a two-temperature distribution function, then both temperatures are indicated. In our paper, we used data from the front* and rear electron spectrometers, correspondingly.

Reference	Year	Target	E_{tot} (J)	I (10^{15} W/cm^2)	T_h (keV)	η (%)
10	2014	Massive Cu or Al	290–580	50	>50	2–7
29	2016	Cu foil + massive	440	20	29^{+8}_{-4}	0.11–0.23
11	2018	Layered CHTiCu	650	10	30 ± 9	$5.32^{+6.9}_{-0.26}$
60	2019	Layered CHTi	700	10	40 ± 5 / 85 ± 5	3.5 ± 0.5 / 1.8 ± 0.5
22	2019	Layered CHTiAl	650	10	58 ± 10	5.3 ± 2
43	2020	Massive Cu + plastic	500	10	58 ± 10	0.6–3
This work	2023	Different ablators + PP + Cu + CH	600	3–15	35 ± 7 / 70 ± 20*	$0.9^{+0.8}_{-0.5}$

Refs. 10, 43, 65, and 68, i.e., the backward-propagating electron flow is strongly affected by the MG-scale spontaneous azimuthal magnetic fields and is reflected back to the target. However, the direction and energy distribution of reflected HEs should also be investigated because the topology of these fields is quite complicated.

The experiments conducted at other laser facilities (e.g., Omega[34,58,70] and NIF[59]) typically have distinct interaction conditions, and so different mechanisms of HE generation could be involved.[71–80] However, note that the conversion efficiency measured in our experiment is similar to the typical values measured elsewhere,[34,58,59] while the electron temperature can be different. In our experiment, we suggest that HEs are mainly produced by SRS instabilities; see Ref. 32. This is indicated by the fact that the HE temperature measured here is consistent with the phase velocity of electron plasma waves produced by SRS.

IV. CONCLUSIONS

Herein, we used a combined approach with a longer laser wavelength in the IR range, high laser intensities exceeding 10^{16} W/cm^2, and thin multilayer targets to study the generation of HEs under SI-relevant conditions. These conditions lead to strong LPI and HEs, giving a better understanding of the physics of HE production in the forward and backward directions, as well as the possibility of using longer-wavelength pulses in the spike part of an SI design. We reported a detailed analysis of the data obtained by four different HE diagnostics, namely a BSC, three electron magnetic spectrometers, a time-resolved K$_\alpha$ imaging system, and a time-integrated K$_\alpha$ spectrometer, and we provided an extended discussion of the results. The analysis revealed drawbacks and advantages of each diagnostic, suggesting that their combined use might result in complementary information providing a more complete characterization of HEs generated under ICF conditions.

The results showed that the BSC is a powerful diagnostic for determining the temporally and spatially integrated energy distribution, temperature, and conversion efficiency of the HEs propagating through the target. Analyzing the experimental data requires Monte Carlo simulations of the electron transport into the target with an accurate geometry of the laser–target interaction conditions. Electron magnetic spectrometers provide a simple-to-use but very effective method for direct temporally integrated and angularly resolved measurements of the energy distribution of the HEs. The narrow angular window of this diagnostic also offers a tool for investigating the divergence and anisotropic features of the HEs. In our experiment, for example, different energy distributions are found for HEs propagating in the forward and backward directions, suggesting different generation mechanisms. When electron spectrometers are located behind the target, caution is needed to account for the energy- and material-dependent stopping power of the target, which results in a measured energy distribution and therefore temperature of the HEs that can differ significantly from those describing the HEs observed on the front side. Therefore, correct use of the diagnostics requires proper correction of the raw data relying on Monte Carlo simulations; alternatively, targets thinner than the stopping range of electrons with the expected temperature/energy should be used in combination with an experimental setup with a spectral energy cutoff able to reduce the effects of magnetic and sheath fields on the electron trajectories.

K$_\alpha$ imaging and spectrometer systems can be used in both the time-resolved and time-integrating mode, thus providing valuable information about the production of HEs; this configuration can be of primary importance for determining the impact of the HE kinetics on the fuel compression, or if combined with a time-resolved LPI diagnostic, it can be a significant tool for understand their origin. A major difficulty in using these diagnostics is reliable subtraction of the x-ray background produced mainly by the bremsstrahlung and recombination emission of the plasma corona, which can be comparable to and in some cases even surmount the intensity of the K$_\alpha$ line. While the background continuum intensity can be easily quantified and therefore subtracted from the total intensity by using a K$_\alpha$ spectrometer, correct quantification of the continuum contribution can be quite tricky for an imaging system and needs dedicated measurements or simulations. An additional difficulty of the imaging system is the spectral range of the x-ray acquisition, which is limited by the crystal size and optical setup. In fact, in some cases the spectral range can make it impossible to acquire the entire K$_\alpha$ line shape, which is because of the temperature dependence of the K$_\alpha$ width and central wavelength, but this does not influence the determination of the HE rising edge timing vs the laser profile. Nevertheless, the K$_\alpha$ imaging system is the favorite diagnostic for investigating the divergence and spatial features of HEs.

The present results provided an electron temperatures of ~35 keV and a laser-to-HE conversion efficiency of 1%–2%. These values are consistent with detailed simulations done with the CHIC code[60] at $\lambda = 1.315$ μm and a laser intensity of 10^{16} W/cm^2, as well as with experimental data collected under similar conditions from the front and rear sides of the target.[10,22,43] Implementing a comprehensive set of multiple diagnostics as reported herein is very important for future studies focused on understanding HE generation and transport in ICF-scale targets and their relationship to laser plasma instabilities.

AUTHOR DECLARATIONS

Conflict of Interest

The authors have no conflicts to disclose.

Author Contributions

Evgeny Filippov: Data curation (equal); Formal analysis (equal); Investigation (equal); Project administration (equal); Writing – original draft (equal); Writing – review & editing (equal). **Matthew Khan**: Data curation (equal); Formal analysis (equal); Investigation (equal); Writing – review & editing (equal). **Alessandro Tentori**: Data curation (equal); Formal analysis (equal); Investigation (equal); Writing – review & editing (equal). **Pavel Gajdos**: Data curation (equal); Formal analysis (equal); Investigation (equal). **Artem Sergeevich Martynenko**: Data curation (equal); Formal analysis (equal); Investigation (equal). **Roman Dudzak**: Data curation (equal); Formal analysis (equal); Investigation (equal). **Petra Koester**: Formal analysis (equal); Investigation (equal). **Ghassan Zeraouli**: Data curation (equal); Formal analysis (equal); Investigation (equal). **Donaldi Mancelli**: Data curation (equal); Formal analysis (equal); Investigation (equal). **Federica Baffigi**: Formal analysis (equal). **Leonida Antonio Gizzi**: Conceptualization (equal); Project administration (equal); Writing – review & editing (equal). **Sergey Pikuz**: Formal analysis (equal); Funding acquisition (equal); Supervision (equal). **Philippe Dominique Nicolai**: Data curation (equal); Investigation (equal); Validation (equal). **Nigel C. Woolsey**: Data curation (equal); Formal analysis (equal); Investigation (equal); Supervision (equal). **Robert Fedosejevs**: Data curation (equal); Formal analysis (equal); Investigation (equal); Supervision (equal); Writing – review & editing (equal). **Miroslav Krus**: Investigation (equal); Project administration (equal); Resources (equal). **Libor Juha**: Investigation (equal); Project administration (equal); Resources (equal). **Dimitri Batani**: Conceptualization (equal); Data curation (equal); Formal analysis (equal); Funding acquisition (equal); Investigation (equal); Project administration (equal); Supervision (lead); Writing – review & editing (equal). **Oldrich Renner**: Conceptualization (equal); Data curation (equal); Formal analysis (equal); Investigation (equal); Methodology (equal); Resources (equal); Supervision (equal); Writing – review & editing (equal). **Gabriele Cristoforetti**: Conceptualization (lead); Data curation (equal); Formal analysis (equal); Funding acquisition (equal); Investigation (equal); Methodology (equal); Project administration (lead); Supervision (equal); Writing – original draft (equal); Writing – review & editing (equal).

DATA AVAILABILITY

The data that support the findings of this study are available on a reasonable request from the corresponding author.

REFERENCES

[1] S. Atzeni, X. Ribeyre, G. Schurtz, A. J. Schmitt, B. Canaud, R. Betti, and L. J. Perkins, "Shock ignition of thermonuclear fuel: Principles and modelling," Nucl. Fusion **54**, 054008 (2014).

[2] R. Betti, C. D. Zhou, K. S. Anderson, L. J. Perkins, W. Theobald, and A. A. Solodov, "Shock ignition of thermonuclear fuel with high areal density," Phys. Rev. Lett. **98**, 155001 (2007).

[3] V. Shcherbakov, "Ignition of a laser-fusion target by a focusing shock wave," Sov. J. Plasma Phys **9**(2), 240–241 (1983).

[4] D. Batani, S. Baton, A. Casner, S. Depierreux, M. Hohenberger, O. Klimo, M. Koenig, C. Labaune, X. Ribeyre, C. Rousseaux, G. Schurtz, W. Theobald, and V. T. Tikhonchuk, "Physics issues for shock ignition," Nucl. Fusion **54**, 054009 (2014).

[5] H. A. Baldis, D. S. Montgomery, J. D. Moody, C. Labaune, S. H. Batha, K. G. Estabrook, R. L. Berger, and W. L. Kruer, "Parametric instabilities in large nonuniform laser plasmas," Plasma Phys. Controlled Fusion **34**, 2077 (1992).

[6] B. B. Afeyan and E. A. Williams, "Stimulated Raman sidescattering with the effects of oblique incidence," Phys. Fluids **28**, 3397 (1985).

[7] C. S. Liu and M. N. Rosenbluth, "Parametric decay of electromagnetic waves into two plasmons and its consequences," Phys. Fluids **19**, 967 (2008).

[8] A. Colaïtis, X. Ribeyre, E. Le Bel, G. Duchateau, P. Nicolaï, and V. Tikhonchuk, "Influence of laser induced hot electrons on the threshold for shock ignition of fusion reactions," Phys. Plasmas **23**, 072703 (2016).

[9] S. Gus'kov, X. Ribeyre, M. Touati, J. L. Feugeas, P. Nicolaï, and V. Tikhonchuk, "Ablation pressure driven by an energetic electron beam in a dense plasma," Phys. Rev. Lett. **109**, 255004 (2012).

[10] S. Y. Gus'Kov, N. N. Demchenko, A. Kasperczuk, T. Pisarczyk, Z. Kalinowska, T. Chodukowski, O. Renner, M. Smid, E. Krousky, M. Pfeifer, J. Skala, J. Ullschmied, and P. Pisarczyk, "Laser-driven ablation through fast electrons in PALS-experiment at the laser radiation intensity of 1–50 PW/cm^2," Laser Part. Beams **32**, 177–195 (2014).

[11] D. Batani, L. Antonelli, F. Barbato, G. Boutoux, A. Colaïtis, J. L. Feugeas, G. Folpini, D. Mancelli, P. Nicolai, J. Santos, J. Trela, V. Tikhonchuk, J. Badziak, T. Chodukowski, K. Jakubowska, Z. Kalinowska, T. Pisarczyk, M. Rosinski, M. Sawicka, F. Baffigi, G. Cristoforetti, F. D'Amato, P. Koester, L. A. Gizzi, S. Viciani, S. Atzeni, A. Schiavi, M. Skoric, S. Gus'Kov, J. Honrubia, J. Limpouch, O. Klimo, J. Skala, Y. J. Gu, E. Krousky, O. Renner, M. Smid, S. Weber, R. Dudzak, M. Krus, and J. Ullschmied, "Progress in understanding the role of hot electrons for the shock ignition approach to inertial confinement fusion," Nucl. Fusion **59**, 032012 (2018).

[12] R. Betti, W. Theobald, C. D. Zhou, K. S. Anderson, P. W. McKenty, S. Skupsky, D. Shvarts, V. N. Goncharov, J. A. Delettrez, P. B. Radha, T. C. Sangster, C. Stoeckl, and D. D. Meyerhofer, "Shock ignition of thermonuclear fuel with high areal densities," J. Phys.: Conf. Ser. **112**, 022024 (2008).

[13] R. K. Kirkwood, J. D. Moody, J. Kline, E. Dewald, S. Glenzer, L. Divol, P. Michel, D. Hinkel, R. Berger, E. Williams, J. Milovich, L. Yin, H. Rose, B. Macgowan, O. Landen, M. Rosen, and J. Lindl, "A review of laser–plasma interaction physics of indirect-drive fusion," Plasma Phys. Controlled Fusion **55**, 103001 (2013).

[14] R. S. Craxton, K. S. Anderson, T. R. Boehly, V. N. Goncharov, D. R. Harding, J. P. Knauer, R. L. McCrory, P. W. McKenty, D. D. Meyerhofer, J. F. Myatt, A. J. Schmitt, J. D. Sethian, R. W. Short, S. Skupsky, W. Theobald, W. L. Kruer, K. Tanaka, R. Betti, T. J. Collins, J. A. Delettrez, S. X. Hu, J. A. Marozas, A. V. Maximov, D. T. Michel, P. B. Radha, S. P. Regan, T. C. Sangster, W. Seka, A. A. Solodov, J. M. Soures, C. Stoeckl, and J. D. Zuegel, "Direct-drive inertial confinement fusion: A review," Phys. Plasmas **22**, 110501 (2015).

[15] J. R. Fein, J. P. Holloway, M. R. Trantham, P. A. Keiter, D. H. Edgell, D. H. Froula, D. Haberberger, Y. Frank, M. Fraenkel, E. Raicher, R. Shvarts, and R. P. Drake, "Mitigation of hot electrons from laser-plasma instabilities in high-z, highly ionized plasmas," Phys. Plasmas **24**, 032707 (2017).

[16] R. H. Scott, K. Glize, L. Antonelli, M. Khan, W. Theobald, M. Wei, R. Betti, C. Stoeckl, A. G. Seaton, T. D. Arber, D. Barlow, T. Goffrey, K. Bennett, W. Garbett, S. Atzeni, A. Casner, D. Batani, C. Li, and N. Woolsey, "Shock ignition

laser-plasma interactions in ignition-scale plasmas," Phys. Rev. Lett. **127**, 065001 (2021).

[17]H. H. Ma, X. F. Li, S. M. Weng, S. H. Yew, S. Kawata, P. Gibbon, Z. M. Sheng, and J. Zhang, "Mitigating parametric instabilities in plasmas by sunlight-like lasers," Matter Radiat. Extremes **6**, 055902 (2021).

[18]J. Breil, S. Galera, and P. H. Maire, "Multi-material ALE computation in inertial confinement fusion code CHIC," Comput. Fluids **46**, 161–167 (2011).

[19]H. Azechi, H. Shiraga, N. Miyanaga, and H. Nishimura, "Review of icf plasma diagnostics," Fusion Eng. Des. **34-35**, 37–44 (1997), part of Special Issue on Fusion Plasma Diagnostics.

[20]H. Nishimura, H. Niki, N. Miyanaga, K. Okada, H. Azechi, T. Yabe, R. Tsuji, S. Ido, M. Yamanaka, T. Mochizuki, K. Nishihara, T. Yamanaka, and C. Yamanaka, "X-ray and radioactive measurements in icf research at ile Osaka (invited)," Rev. Sci. Instrum. **56**, 1128–1132 (1985).

[21]A. Y. Faenov, S. A. Pikuz, A. I. Erko, B. A. Bryunetkin, V. M. Dyakin, G. V. Ivanenkov, A. R. Mingaleev, T. A. Pikuz, V. M. Romanova, and T. A. Shelkovenko, "High-performance x-ray spectroscopic devices for plasma microsources investigations," Phys. Scr. **50**, 333–338 (1994).

[22]G. Cristoforetti, L. Antonelli, D. Mancelli, S. Atzeni, F. Baffigi, F. Barbato, D. Batani, G. Boutoux, F. D'Amato, J. Dostal *et al.*, "Time evolution of stimulated Raman scattering and two-plasmon decay in laser-produced plasma relevant for shock ignition in a hot plasma," High Power Laser Sci. Eng. **7**, e51 (2019).

[23]A. Visco, R. P. Drake, D. H. Froula, S. H. Glenzer, and B. B. Pollock, "Temporal dispersion of a spectrometer," Rev. Sci. Instrum. **79**, 10F545 (2008).

[24]D. Haberberger, S. Ivancic, S. X. Hu, R. Boni, M. Barczys, R. S. Craxton, and D. H. Froula, "Measurements of electron density profiles using an angular filter refractometer," Phys. Plasmas **21**, 056304 (2014).

[25]O. V. Gotchev, P. Brijesh, P. M. Nilson, C. Stoeckl, and D. D. Meyerhofer, "A compact, multiangle electron spectrometer for ultraintense laser-plasma interaction experiments," Rev. Sci. Instrum. **79**, 053505 (2008).

[26]T. Pisarczyk, O. Renner, R. Dudzak, T. Chodukowski, Z. Rusiniak, J. Domanski, J. Badziak, J. Dostal, M. Krupka, S. Singh, D. Klir, M. Ehret, P. Gajdos, A. Zaras-Szydłowska, M. Rosinski, P. Tchórz, M. Szymanski, J. Krasa, T. Burian, M. Pfeifer, J. Cikhardt, S. Jelinek, G. Kocourkova, D. Batani, K. Batani, J. Santos, C. Vlachos, V. Ospina-Bohórquez, L. Volpe, S. Borodziuk, M. Krus, and L. Juha, "Influence of the magnetic field on properties of hot electron emission from ablative plasma produced at laser irradiation of a disc-coil target," Plasma Phys. Controlled Fusion **64**, 115012 (2022).

[27]M. Krupka, S. Singh, T. Pisarczyk, J. Dostal, M. Kalal, J. Krasa, R. Dudzak, T. Burian, S. Jelinek, T. Chodukowski, Z. Rusiniak, M. Krus, and L. Juha, "Design of modular multi-channel electron spectrometers for application in laser matter interaction experiments at Prague Asterix Laser System," Rev. Sci. Instrum. **92**, 023514 (2021).

[28]A. G. MacPhee, K. U. Akli, F. N. Beg, C. D. Chen, H. Chen, R. Clarke, D. S. Hey, R. R. Freeman, A. J. Kemp, M. H. Key, J. A. King, S. Le Pape, A. Link, T. Y. Ma, H. Nakamura, D. T. Offermann, V. M. Ovchinnikov, P. K. Patel, T. W. Phillips, R. B. Stephens, R. Town, Y. Y. Tsui, M. S. Wei, L. D. Van Woerkom, and A. J. MacKinnon, "Diagnostics for fast ignition science (invited)," Rev. Sci. Instrum. **79**, 10F302 (2008).

[29]O. Renner, M. Šmíd, D. Batani, and L. Antonelli, "Suprathermal electron production in laser-irradiated Cu targets characterized by combined methods of x-ray imaging and spectroscopy," Plasma Phys. Controlled Fusion **58**, 075007 (2016).

[30]K. Jungwirth, A. Cejnarova, L. Juha, B. Kralikova, J. Krasa, E. Krousky, P. Krupickova, L. Laska, K. Masek, T. Mocek, M. Pfeifer, A. Präg, O. Renner, K. Rohlena, B. Rus, J. Skala, P. Straka, and J. Ullschmied, "The Prague Asterix Laser System," Phys. Plasmas **8**, 2495 (2001).

[31]W. Theobald, A. Bose, R. Yan, R. Betti, M. Lafon, D. Mangino, A. R. Christopherson, C. Stoeckl, W. Seka, W. Shang, D. T. Michel, C. Ren, R. C. Nora, A. Casner, J. Peebles, F. N. Beg, X. Ribeyre, E. Llor Aisa, A. Colaïtis, V. Tikhonchuk, and M. S. Wei, "Enhanced hot-electron production and strong-shock generation in hydrogen-rich ablators for shock ignition," Phys. Plasmas **24**, 120702 (2017).

[32]G. Cristoforetti , "Investigation on hot electron origin in laser plasma interaction at shock ignition intensities," Sci. Rep (submitted) (2023).

[33]C. D. Chen, J. A. King, M. H. Key, K. U. Akli, F. N. Beg, H. Chen, R. R. Freeman, A. Link, A. J. MacKinnon, A. G. MacPhee, P. K. Patel, M. Porkolab, R. B. Stephens, and L. D. Van Woerkom, "A Bremsstrahlung spectrometer using k-edge and differential filters with image plate dosimeters," Rev. Sci. Instrum. **79**, 10E305 (2008).

[34]A. Tentori, A. Colaitis, W. Theobald, A. Casner, D. Raffestin, A. Ruocco, J. Trela, E. Le Bel, K. Anderson, M. Wei, B. Henderson, J. Peebles, R. Scott, S. Baton, S. A. Pikuz, R. Betti, M. Khan, N. Woolsey, S. Zhang, and D. Batani, "Experimental characterization of hot-electron emission and shock dynamics in the context of the shock ignition approach to inertial confinement fusion," Phys. Plasmas **28**, 103302 (2021).

[35]P. Koester, F. Baffigi, G. Cristoforetti, L. Labate, L. A. Gizzi, S. Baton, M. Koenig, A. Colaïtis, D. Batani, A. Casner, D. Raffestin, A. Tentori, J. Trela, C. Rousseaux, G. Boutoux, S. Brygoo, J. Jacquet, C. Reverdin, E. Le Bel, L. Le-Deroff, W. Theobald, and K. Shigemori, "Bremsstrahlung cannon design for shock ignition relevant regime," Rev. Sci. Instrum. **92**, 013501 (2021).

[36]J. Ayers and J. Ladell, "Spectral widths of the Cu Kα lines," Phys. Rev. A **37**, 2404 (1988).

[37]O. Renner "Time resolved generation of hot electrons at shock ignition relevant laser coupling parameters," (to be published) (2023).

[38]I. J. Paterson, R. J. Clarke, N. C. Woolsey, and G. Gregori, "Image plate response for conditions relevant to laser–plasma interaction experiments," Meas. Sci. Technol. **19**, 095301 (2008).

[39]G. Boutoux, D. Batani, F. Burgy, J. E. Ducret, P. Forestier-Colleoni, S. Hulin, N. Rabhi, A. Duval, L. Lecherbourg, C. Reverdin, K. Jakubowska, C. I. Szabo, S. Bastiani-Ceccotti, F. Consoli, A. Curcio, R. De Angelis, F. Ingenito, J. Baggio, and D. Raffestin, "Validation of modelled imaging plates sensitivity to 1-100 keV x-rays and spatial resolution characterisation for diagnostics for the 'PETawatt Aquitaine Laser'," Rev. Sci. Instrum. **87**, 043108 (2016).

[40]A. Colaïtis, G. Duchateau, X. Ribeyre, Y. Maheut, G. Boutoux, L. Antonelli, P. Nicolaï, D. Batani, and V. Tikhonchuk, "Coupled hydrodynamic model for laser-plasma interaction and hot electron generation," Phys. Rev. E **92**, 041101 (2015).

[41]A. Tentori, A. Colaïtis, D. Batani, and A. Colaïtis, "3D Monte-Carlo model to study the transport of hot electrons in the context of inertial confinement fusion. Part I," Matter Radiat. Extremes **7**, 065902 (2022).

[42]A. Tentori, A. Colaïtis, D. Batani, and A. Colaïtis, "3D Monte-Carlo model to study the transport of hot electrons in the context of inertial confinement fusion. Part II," Matter Radiat. Extremes **7**, 065903 (2022).

[43]T. Pisarczyk, M. Kalal, S. Y. Gus'kov, D. Batani, O. Renner, J. Santos, R. Dudzak, A. Zaras-Szydłowska, T. Chodukowski, Z. Rusiniak, J. Dostal, J. Krasa, M. Krupka, I. Kochetkov, S. Singh, J. Cikhardt, T. Burian, M. Krus, M. Pfeifer, G. Cristoforetti, L. A. Gizzi, F. Baffigi, L. Antonelli, N. N. Demchenko, M. Rosinski, D. Terwińska, S. Borodziuk, P. Kubes, M. Ehret, L. Juha, J. Skala, and P. Korneev, "Hot electron retention in laser plasma created under terawatt subnanosecond irradiation of cu targets," Plasma Phys. Controlled Fusion **62**, 115020 (2020).

[44]H. Schmitz, "Target normal sheath acceleration sheath fields for arbitrary electron energy distribution," Phys. Plasmas **19**, 083115 (2012).

[45]G. Cristoforetti, L. Antonelli, S. Atzeni, F. Baffigi, F. Barbato, D. Batani, G. Boutoux, A. Colaitis, J. Dostal, R. Dudzak, L. Juha, P. Koester, A. Marocchino, D. Mancelli, P. Nicolai, O. Renner, J. J. Santos, A. Schiavi, M. M. Skoric, M. Smid, P. Straka, and L. A. Gizzi, "Measurements of parametric instabilities at laser intensities relevant to strong shock generation," Phys. Plasmas **25**, 012702 (2018).

[46]W. Theobald, R. Nora, M. Lafon, A. Casner, X. Ribeyre, K. S. Anderson, R. Betti, J. A. Delettrez, J. A. Frenje, V. Y. Glebov, O. V. Gotchev, M. Hohenberger, S. X. Hu, F. J. Marshall, D. D. Meyerhofer, T. C. Sangster, G. Schurtz, W. Seka, V. A. Smalyuk, C. Stoeckl, and B. Yaakobi, "Spherical shock-ignition experiments with the 40 + 20-beam configuration on omega," Phys. Plasmas **19**, 102706 (2012).

[47]O. Klimo, J. Psikal, V. T. Tikhonchuk, and S. Weber, "Two-dimensional simulations of laser–plasma interaction and hot electron generation in the context of shock-ignition research," Plasma Phys. Controlled Fusion **56**, 055010 (2014).

[48]C. Z. Xiao, Z. J. Liu, C. Y. Zheng, and X. T. He, "Competition between stimulated Raman scattering and two-plasmon decay in inhomogeneous plasma," Phys. Plasmas **23**, 022704 (2016).

[49]F. N. Beg, A. R. Bell, A. E. Dangor, C. N. Danson, A. P. Fews, M. E. Glinsky, B. A. Hammel, P. Lee, P. A. Norreys, and M. Tatarakis, "A study of picosecond laser–solid interactions up to 10^{19} W cm^{-2}," Phys. Plasmas **4**, 447–457 (1997).

[50]K. Estabrook and W. L. Kruer, "Properties of resonantly heated electron distributions," Phys. Rev. Lett. **40**, 42–45 (1978).

[51]S. Wilks and W. Kruer, "Absorption of ultrashort, ultra-intense laser light by solids and overdense plasmas," IEEE J. Quantum Electron. **33**, 1954–1968 (1997).

[52]A. Pukhov, Z. M. Sheng, and J. Meyer-ter Vehn, "Particle acceleration in relativistic laser channels," Phys. Plasmas **6**, 2847 (1999).

[53]P. Korneev, E. D'Humières, and V. Tikhonchuk, "Gigagauss-scale quasistatic magnetic field generation in a snail-shaped target," Phys. Rev. E **91**, 043107 (2015).

[54]A. V. Brantov, P. Korneev, and V. Y. Bychenkov, "Magnetic field generation from a coil-shaped foil by a laser-triggered hot-electron current," Laser Phys. Lett. **16**, 066006 (2019).

[55]V. T. Tikhonchuk, M. Bailly-Grandvaux, J. J. Santos, and A. Poyé, "Quasistationary magnetic field generation with a laser-driven capacitor-coil assembly," Phys. Rev. E **96**, 023202 (2017).

[56]O. Klimo and V. T. Tikhonchuk, "Laser–plasma interaction studies in the context of shock ignition: The regime dominated by parametric instabilities," Plasma Phys. Controlled Fusion **55**, 095002 (2013).

[57]H. T. Kim, K. H. Pae, H. J. Cha, I. J. Kim, T. J. Yu, J. H. Sung, S. K. Lee, T. M. Jeong, and J. Lee, "Enhancement of electron energy to the multi-gev regime by a dual-stage laser-wakefield accelerator pumped by petawatt laser pulses," Phys. Rev. Lett. **111**, 165002 (2013).

[58]S. Zhang, C. M. Krauland, J. Peebles, J. Li, F. N. Beg, N. Alexander, W. Theobald, R. Betti, D. Haberberger, E. M. Campbell, R. Yan, E. Borwick, C. Ren, and M. S. Wei, "Experimental study of hot electron generation in shock ignition relevant high-intensity regime with large scale hot plasmas," Phys. Plasmas **27**, 023111 (2020).

[59]M. J. Rosenberg, A. A. Solodov, J. F. Myatt, W. Seka, P. Michel, M. Hohenberger, R. W. Short, R. Epstein, S. P. Regan, E. M. Campbell, T. Chapman, C. Goyon, J. E. Ralph, M. A. Barrios, J. D. Moody, and J. W. Bates, "Origins and scaling of hot-electron preheat in ignition-scale direct-drive inertial confinement fusion experiments," Phys. Rev. Lett. **120**, 055001 (2018).

[60]L. Antonelli, J. Trela, F. Barbato, G. Boutoux, P. Nicolaï, D. Batani, V. Tikhonchuk, D. Mancelli, A. Tentori, S. Atzeni, A. Schiavi, F. Baffigi, G. Cristoforetti, S. Viciani, L. A. Gizzi, M. Smid, O. Renner, J. Dostal, R. Dudzak, L. Juha, and M. Krus, "Laser-driven strong shocks with infrared lasers at intensity of 10^{16} W/cm^2," Phys. Plasmas **26**, 112708 (2019).

[61]H. K. Chung, M. H. Chen, W. L. Morgan, Y. Ralchenko, and R. W. Lee, "FLYCHK: Generalized population kinetics and spectral model for rapid spectroscopic analysis for all elements," High Energy Density Phys. **1**, 3–12 (2005).

[62]X. Llovet, C. J. Powell, F. Salvat, and A. Jablonski, "Cross sections for inner-shell ionization by electron impact," J. Phys. Chem. Ref. Data **43**, 013102 (2014).

[63]S. T. Perkins, D. E. Cullen, M. H. Chen, J. Rathkopf, J. Scofield, and J. H. Hubbell, "Tables and graphs of atomic subshell and relaxation data derived from the LLNL Evaluated Atomic Data Library (EADL), Z = 1–100," Technical Report UCRL-50400-Vol. 30, Lawrence Livermore National Laboratory (LLNL), 1991.

[64]D. Batani, L. Antonelli, S. Atzeni, J. Badziak, F. Baffigi, T. Chodukowski, F. Consoli, G. Cristoforetti, R. De Angelis, R. Dudzak, G. Folpini, L. Giuffrida, L. A. Gizzi, Z. Kalinowska, P. Koester, E. Krousky, M. Krus, L. Labate, T. Levato, Y. Maheut, G. Malka, D. Margarone, A. Marocchino, J. Nejdl, P. Nicolai, T. O'Dell, T. Pisarczyk, O. Renner, Y. J. Rhee, X. Ribeyre, M. Richetta, M. Rosinski, M. Sawicka, A. Schiavi, J. Skala, M. Smid, C. Spindloe, J. Ullschmied, A. Velyhan, and T. Vinci, "Generation of high pressure shocks relevant to the shock-ignition intensity regime," Phys. Plasmas **21**, 032710 (2014).

[65]T. Pisarczyk, S. Y. Gus'kov, R. Dudzak, T. Chodukowski, J. Dostal, N. N. Demchenko, P. Korneev, Z. Kalinowska, M. Kalal, O. Renner, M. Smid, S. Borodziuk, E. Krousky, J. Ullschmied, J. Hrebicek, T. Medrik, J. Golasowski, M. Pfeifer, J. Skala, and P. Pisarczyk, "Space-time resolved measurements of spontaneous magnetic fields in laser-produced plasma," Phys. Plasmas **22**, 102706 (2015).

[66]J. Trela, W. Theobald, K. S. Anderson, D. Batani, R. Betti, A. Casner, J. A. Delettrez, J. A. Frenje, V. Y. Glebov, X. Ribeyre, A. A. Solodov, M. Stoeckl, and C. Stoeckl, "The control of hot-electron preheat in shock-ignition implosions," Phys. Plasmas **25**, 052707 (2018).

[67]G. Cristoforetti, A. Colaïtis, L. Antonelli, S. Atzeni, F. Baffigi, D. Batani, F. Barbato, G. Boutoux, R. Dudzak, P. Koester, E. Krousky, L. Labate, P. Nicolaï, O. Renner, M. Skoric, V. Tikhonchuk, and L. A. Gizzi, "Experimental observation of parametric instabilities at laser intensities relevant for shock ignition," EPL (Europhys. Lett.) **117**, 35001 (2017).

[68]T. Pisarczyk, S. Y. Gus'kov, T. Chodukowski, R. Dudzak, P. Korneev, N. N. Demchenko, Z. Kalinowska, J. Dostal, A. Zaras-Szydlowska, S. Borodziuk, L. Juha, J. Cikhardt, J. Krasa, B. Cikhardtova, P. Kubes, E. Krousky, M. Krus, J. Ullschmied, K. Jungwirth, J. Hrebicek, T. Medrik, J. Golasowski, M. Pfeifer, O. Renner, S. Singh, S. Kar, H. Ahmed, J. Skala, and P. Pisarczyk, "Kinetic magnetization by fast electrons in laser-produced plasmas at sub-relativistic intensities," Phys. Plasmas **24**, 102711 (2017).

[69]A. A. Solodov, M. J. Rosenberg, W. Seka, J. F. Myatt, M. Hohenberger, R. Epstein, C. Stoeckl, R. W. Short, S. P. Regan, P. Michel, T. Chapman, R. K. Follett, J. P. Palastro, D. H. Froula, P. B. Radha, J. D. Moody, and V. N. Goncharov, "Hot-electron generation at direct-drive ignition-relevant plasma conditions at the National Ignition Facility," Phys. Plasmas **27**, 052706 (2020).

[70]M. Hohenberger, W. Theobald, S. X. Hu, K. S. Anderson, R. Betti, T. R. Boehly, A. Casner, D. E. Fratanduono, M. Lafon, D. D. Meyerhofer, R. Nora, X. Ribeyre, T. C. Sangster, G. Schurtz, W. Seka, C. Stoeckl, and B. Yaakobi, "Shock-ignition relevant experiments with planar targets on OMEGA," Phys. Plasmas **21**, 022702 (2014).

[71]C. Zulick, B. Hou, F. Dollar, A. Maksimchuk, J. Nees, A. G. R. Thomas, Z. Zhao, and K. Krushelnick, "High resolution bremsstrahlung and fast electron characterization in ultrafast intense laser–solid interactions," New J. Phys. **15**, 123038 (2013).

[72]M. D. Rosen, "Scaling laws for femtosecond laser-plasma interactions," Proc. SPIE **1229**, 160–169 (1990).

[73]S. C. Wilks, A. B. Langdon, T. E. Cowan, M. Roth, M. Singh, S. Hatchett, M. H. Key, D. Pennington, A. MacKinnon, and R. A. Snavely, "Energetic proton generation in ultra-intense laser-solid interactions," Phys. Plasmas **8**, 542–549 (2001).

[74]P. Gibbon, *Short Pulse Laser Interactions with Matter: An Introduction* (Imperial College Press, 2005), pp. 1–312.

[75]B. L. Henke, E. M. Gullikson, and J. C. Davis, "X-ray interactions: Photoabsorption, scattering, transmission, and reflection at E = 50-30 000 eV, Z = 1-92," At. Data Nucl. Data Tables **54**, 181–342 (1993).

[76]S. N. Ryazantsev, A. S. Martynenko, M. V. Sedov, I. Y. Skobelev, M. D. Mishchenko, Y. S. Lavrinenko, C. D. Baird, N. Booth, P. Durey, L. N. K. Döhl, D. Farley, K. L. Lancaster, P. McKenna, C. D. Murphy, T. A. Pikuz, C. Spindloe, N. Woolsey, and S. A. Pikuz, "Absolute keV X-ray yield and conversion efficiency in over dense Si sub-petawatt laser plasma," Plasma Phys. Controlled Fusion **64**, 105016 (2022); arXiv:2112.10757v1.

[77]S. Baton, A. Colaïtis, C. Rousseaux, G. Boutoux, S. Brygoo, L. Jacquet, M. Koenig, D. Batani, A. Casner, E. L. Bel, D. Raffestin, A. Tentori, V. Tikhonchuk, J. Trela, C. Reverdin, L. Le-Deroff, W. Theobald, G. Cristoforetti, L. Gizzi, P. Koester, L. Labate, and K. Shigemori, "Preliminary results from the lmj-petal experiment on hot electrons characterization in the context of shock ignition," High Energy Density Phys. **36**, 100796 (2020).

[78]W. Shang, J. Yang, W. Zhang, Z. Li, B. Deng, Y. Dong, T. Zhu, C. Huang, X. Zhan, Y. Mei, L. Guo, R. Yu, S. Li, S. Jiang, S. Liu, F. Wang, Y. Ding, B. Zhang, and R. Betti, "Experimental demonstration of laser to x-ray conversion enhancements with low density gold targets," Appl. Phys. Lett. **108**, 064102 (2016).

[79]B. Soom, R. Weber, and J. E. Balmer, "X-ray conversion efficiency in Cu plasma produced by subnanosecond laser pulses," J. Appl. Phys. **68**, 1392–1394 (1990).

[80]C. Thaury, E. Guillaume, A. Lifschitz, K. Ta Phuoc, M. Hansson, G. Grittani, J. Gautier, J. P. Goddet, A. Tafzi, O. Lundh, and V. Malka, "Shock assisted ionization injection in laser-plasma accelerators," Sci. Rep. **5**, 16310 (2015).